



LAWRENCE  
LIVERMORE  
NATIONAL  
LABORATORY

# Optimization Of Phase-Contrast Enhanced X-Ray Imaging Of D-T Layers

Bernard Kozioziemski

July 15, 2005

## Disclaimer

---

This document was prepared as an account of work sponsored by an agency of the United States Government. Neither the United States Government nor the University of California nor any of their employees, makes any warranty, express or implied, or assumes any legal liability or responsibility for the accuracy, completeness, or usefulness of any information, apparatus, product, or process disclosed, or represents that its use would not infringe privately owned rights. Reference herein to any specific commercial product, process, or service by trade name, trademark, manufacturer, or otherwise, does not necessarily constitute or imply its endorsement, recommendation, or favoring by the United States Government or the University of California. The views and opinions of authors expressed herein do not necessarily state or reflect those of the United States Government or the University of California, and shall not be used for advertising or product endorsement purposes.

This work was performed under the auspices of the U.S. Department of Energy by University of California, Lawrence Livermore National Laboratory under Contract W-7405-Eng-48.

*Target Area Technologies Program*

*Mail Station L - 472*

*Ext: 4-6317*

UCRL-TR-?????? June 22, 2005

MEMORANDUM

TO: Distribution

FROM: Bernard Kozioziemski

SUBJECT: Optimization of phase-contrast enhanced x-ray imaging of D-T layers

---

I. SUMMARY

Phase-contrast enhanced x-ray imaging has been demonstrated for characterization of D-T layers inside of beryllium shells. These first demonstrations used both scintillator and direct-detection imaging. This memo details tradeoffs between the two methods in order to optimize the imaging. The guiding principle for optimization is to minimize the exposure time while maximizing the signal-to-noise ratio at the D-T solid-vapor interface. Direct-detection and scintillator performance are comparable when imaging the full capsule. However, a scintillator allows for higher-resolution images necessary for studying local defects in the D-T layer.

II. INTRODUCTION

X-ray phase-contrast enhanced imaging takes advantage of the small refraction and diffraction of x-rays at sharp changes in the integrated density profile. This imaging method has been demonstrated using both scintillator and direct-detection imaging methods. The best results to date were obtained in collaboration with LANL using the direct-detection method, where an x-ray CCD converts the x-rays to digital counts. These direct-detection images required 20 exposures, 6 seconds each, to acquire a signal-to-noise ratio adequate for the D-T layer characterization. The scintillator systems had significantly lower contrast requiring exposure times of 600 seconds for adequate images. This degraded performance was partially due to the x-ray spectrum and spot size of the x-ray source.

This memo calculates the relative performance of a scintillator and direct-detection system to determine the best solution for characterization of the D-T ice. It will be shown that the scintillator can have a similar performance as the direct-detection for imaging the entire capsule. However, the scintillator is the only option for higher resolution imaging or when the source produces a very fast pulse of x-rays, such as with an X-pinch.

This memo describes how the scintillator material, geometry, and collection optics should be chosen to optimize phase-contrast enhanced x-ray imaging of D-T layers. The criteria used in the comparison is the expected signal-to-noise ratio at the D-T solid–vapor interface for identical integration times. The signal-to-noise will be calculated for each of the x-ray imaging system parts. The signal depends on the system resolution, the x-ray spectrum, and the detector response. The noise is calculated assuming that it is dominated by Poisson noise, simply proportional to the square-root of the number of detected x-ray photons. Detector dark-current is neglected since the signal levels will be much larger than the dark-current of a cooled CCD camera.

### A. X-ray imaging geometry

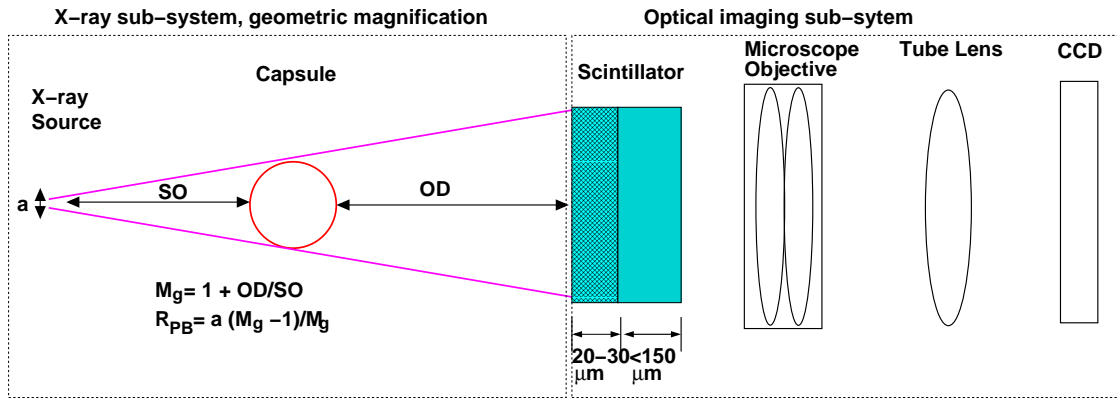


FIG. 1: Layout of a general x-ray imaging system. An x-ray source with FWHM spot-size of  $a$  is placed a distance  $SO$  from the capsule. A detector is located  $OD$  from the capsule, providing a geometric magnification of  $M_g$ . If the detector is a scintillator, it is optically imaged onto a CCD with magnification  $M_o$ . If the detector is a direct-detection x-ray CCD camera, then the scintillator and optical components are replaced by the CCD camera.

Figure 1 shows the x-ray imaging geometry. The x-ray imaging consists of the x-ray imag-

ing sub-system and, if applicable, the optical imaging sub-system. The x-ray imaging sub-system is defined by the source-to-object distance,  $SO$ , and the object-to-detector distance,  $OD$ . The choice of  $SO$  and  $OD$  affect the phase-contrast images in several ways. First, the geometric magnification, defined as  $M_g = 1 + \frac{OD}{SO}$ . Second, the interface contrast due to the phase-contrast enhancement is proportional to the effective plane-wave propagation distance, defined as

$$\begin{aligned} Z_{PW} &= \frac{(OD)(SO)}{OD + SO} \\ &= \frac{OD}{M_g} \\ &= SO \frac{M_g - 1}{M_g}. \end{aligned} \tag{1}$$

The relative performance of different x-ray imaging systems will be compared using identical values of  $Z_{PW}$ .

The penumbral blur is also dependent on the imaging geometry. An x-ray spot size FWHM of  $a$  causes a penumbral blur,  $R_{PB}$ , that depends on  $M_g$  as

$$R_{PB} = a \frac{M_g - 1}{M_g}. \tag{2}$$

As  $M_g$  approaches 1, and the imaging better approximates a plane-wave, the penumbral blur goes to zero. The other limit is for large  $M_g$ , when the penumbral blur approaches the source size. The penumbral blur will be used in determination of the signal at the D-T solid–vapor surface.

### III. X-RAY COLLECTION FACTORS

Micro-focus x-ray sources have limited x-ray photon output. Therefore, it is important to collect as many of the x-rays as possible to decrease the signal-to-noise. This section describes how the number of collected x-ray photons depends on various parts of the x-ray imaging system.

### A. Solid angle

The number of photons collected by a solid angle  $\Omega_x$  is the x-ray flux multiplied by  $\Omega_x$ . A pixel size of  $p_o$  at the object plane subtends a solid angle from to x-ray source of

$$\begin{aligned}\Omega_x &= \frac{p_o^2}{SO^2} \\ &= \frac{p_o^2}{Z_{PW}^2} \frac{(M_g - 1)^2}{M_g^2}.\end{aligned}\tag{3}$$

The exposure time for a given source flux is minimized when  $\Omega_x$  is made as large as possible. Maximizing  $M_g$  for a specified  $Z_{PW}$  will maximize  $\Omega_x$ . However, this conflicts with the need to minimize  $R_{PB}$ . Thus, the choice of  $M_g$  must be made to balance the penumbral blur with the noise level. The noise level, assuming Poisson statistics, scales inversely with  $\Omega_x$ . Table I shows the relative signal-to-noise  $\nu_\Omega$  for a specified  $Z_{PW}$  and  $p_o$ . The signal-to-noise decreases as  $M_g$  approaches 1. Conversely, the required integration time to reach an equivalent signal-to-noise is proportional to  $1/\nu_\Omega^2$ .

TABLE I: Relative signal-to-noise  $\nu_\Omega$  for several geometric magnifications  $M_g$  at constant  $Z_{PW}$  and  $p_o$ .

$M_g$	10	8	5	2	1.5	1.2	1.1
$\nu_\Omega$	0.9	0.875	0.8	0.5	0.33	0.167	0.091

### B. Detector efficiency

The solid angle is only one part of the overall collection efficiency. The relative fraction of x-rays absorbed by the respective detectors also contributes. The x-ray CCD will absorb about 50% of the 8 keV x-rays. For comparison, a 20  $\mu\text{m}$  thick thallium doped CsI scintillator will absorb 90% of the 8 keV x-rays. Six different detector materials will be considered in this paper. One is 30  $\mu\text{m}$  thick Si, which is used in the direct-detection CCD. The remaining five are the following scintillators, 20  $\mu\text{m}$  CsI, 30  $\mu\text{m}$  CsI, 125  $\mu\text{m}$  CsI, 20  $\mu\text{m}$  LSO, and 25  $\mu\text{m}$  LuAG. The CsI has the highest light output and stopping power, but is difficult to make very thin. LSO and LuAG are two different scintillators suggested by vendors.

The emission spectrum was calculated for a Cu-anode source with 45 kV electron accelerating voltage. The relative number of x-ray photons captured by each detector was calculated by integrating the energy dependent absorption over the calculated Cu spectrum. Table II shows the relative number of x-ray photons stopped, where 30  $\mu\text{m}$  Si is defined as 1. These values are denoted as  $\eta$  for the rest of this paper.

TABLE II: Relative number of x-rays stopped,  $\eta$ , by six detectors studied in this paper. The response was calculated for the 45 kV Cu spectrum.

Detector	Si 30 $\mu\text{m}$	CsI 20 $\mu\text{m}$	CsI 30 $\mu\text{m}$	CsI 125 $\mu\text{m}$	LSO 20 $\mu\text{m}$	LuAG 25 $\mu\text{m}$
$\eta$	1	2.35	2.61	3.28	2.87	2.70

While the scintillators stop more of the x-ray photons than Si, not all of the x-rays contribute equally to the signal. Furthermore, the number of x-rays detected by the scintillator depends on both the light output (number of visible photons created for each x-ray photon) and the collection efficiency of the visible optics. The thallium-doped CsI scintillator produces approximately 400 visible light photons (550 nm) for each 8 keV x-ray photon. LSO and LuAG both emit significantly fewer visible light photons.

The fraction of the visible light emitted into  $4\pi$  collected by an optical system of numerical aperture  $NA$  is approximately

$$\Omega_v = (NA)^2/4. \quad (4)$$

Of the 400 visible photons emitted into  $4\pi$ , 9 of those are collected by a 0.3 NA objective. A typical visible light CCD camera has quantum efficiency  $QE$  of 0.4 at 550 nm. With the QE of 0.4, 3.6 visible photons are detected at the CCD for each x-ray photon incident on the scintillator. Other losses in the optical system likely reduce the overall detection efficiency to about 2 detected visible photons per x-ray photon. Using a 0.2 NA objective reduces the detected visible photons to 1 visible photon detected for each x-ray.

It is possible to improve the collection efficiency by using, for instance, a front-illuminated CCD, immersion objectives, or in proper use of anti-reflection coatings on optical components. Therefore, it is reasonable to assume that an optical system using a CsI scintillator can be designed which is capable of detecting 90% of the incident x-ray photons.

### C. Signal levels

As discussed in the previous section, the anode x-ray tube produces K- $\alpha$  x-rays as well as a broad Bremsstrahlung spectrum. Refraction and phase-contrast decreases with increasing x-ray energy. These higher energy x-rays cause reduced contrast and signal-to-noise at the interfaces since they contribute a grey background. However, the scintillator and Si CCD detection efficiency are also functions of the x-ray energy. The signal at the D-T solid–vapor interface, including the detector spectral response, is calculated in this section.

The D-T solid–vapor interface contrast was calculated for several different detector choices to enable comparison and optimization. The x-ray spectrum was calculated for a copper anode with 45 kV electron accelerating voltage and 800  $\mu\text{m}$  of beryllium, consistent with the windows used on our cryostat. The path between the source and detector is assumed to be evacuated to minimize transmission losses through the air path. A later discussion will include the effect of different air paths. The radial intensity line-outs are shown in figure 2, where the pixel size at the object is  $p_o = 2.5 \mu\text{m}$ . The Fresnel calculation was performed for each wavelength and the results were added together with a weighting that depended on the relative source emission and detector absorption. An additional weighting proportional to the x-ray photon energy is included for the scintillating materials since the number of visible photons produced is proportional to the x-ray energy. All runs were normalized to unity outside the Be shell.

The Si CCD chip has the largest signal. Also, thin scintillators perform better than thick scintillators, since the thin scintillator captures fewer high-energy x-rays. The relative signal,  $\delta$ , for each detector is listed in Table III, where the 30  $\mu\text{m}$  Si is defined as 1. Thin CsI scintillators perform nearly as well as the 30  $\mu\text{m}$  thick Si, while a very thick CsI scintillator has a much lower signal. The signal levels will be combined with the number of collected photons in section V to compare their respective signal-to-noise ratios.

TABLE III: Relative signal strengths,  $\delta$ , for several different detectors, where the 30  $\mu\text{m}$  thick Si has been defined as 1.

Detector	Si 30 $\mu\text{m}$	CsI 20 $\mu\text{m}$	CsI 30 $\mu\text{m}$	CsI 125 $\mu\text{m}$	LSO 20 $\mu\text{m}$
$\delta$	1	0.85	0.79	0.58	0.63



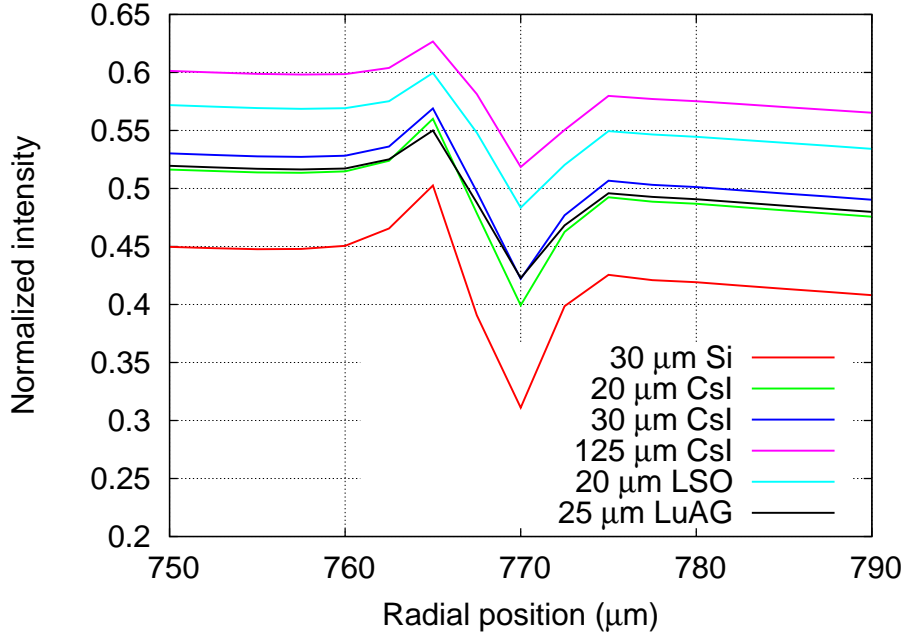


FIG. 2: Radial intensity profiles at the D-T solid-vapor interface calculated with the source spectrum and detector response weighting the spectral range. The pixel pitch is  $2.5 \mu\text{m}$  at the object plane for all traces, and a  $1.2 \mu\text{m}$  FWHM point-spread function was convolved with the data. The signals, defined as the peak-to-valley, are listed in Table III.

#### IV. RESOLUTION

The image contrast and resolvable features depend on the resolution of the x-ray imaging system. This section shows the decrease in the signal at the D-T solid-vapor interface as the point-spread-function is increased. The resolution is limited only by the pixel size and the x-ray spot size, which gives rise to penumbral blurring, for the direct-detection case. The scintillator case must also take into account the optical point-spread-function.

Table IV shows values for the contrast at the D-T solid-vapor interface using 8 keV x-rays with  $Z_{PW} = 50 \text{ mm}$  and  $Z_{PW} = 80 \text{ mm}$  for several different pixel sizes and Gaussian point-spread-function FWHM, referenced to the object plane. As is expected, smaller FWHM blur leads to higher contrast. However, for the largest pixel size of  $2.5 \mu\text{m}$ , the contrast is not significantly improved for FWHM less than  $3.5 \mu\text{m}$ . A factor of 2 improvement in contrast over the  $2.5 \mu\text{m}$  pixel case can be obtained with a  $0.75 \mu\text{m}$  pixel and FWHM of  $1.2 \mu\text{m}$ . Figure 3 shows a radial lineout of the expected intensity profile for these two cases.

TABLE IV: Contrast at the D-T solid-vapor interface for 8 keV x-rays with several different pixel sizes convolved with the FWHM values.

Pixel size ( $\mu\text{m}$ )	$Z_{PW}$ (mm)	FWHM ( $\mu\text{m}$ )				
		1.2	2.3	3.5	4.7	5.9
0.75	50	0.64	0.48	0.32	0.22	0.15
1.5	50	0.49	0.44	0.30	0.16	0.15
2.5	50	0.30	0.30	0.29	0.20	0.14
0.75	80	0.70	0.59	0.44	0.32	0.24
1.5	80	0.69	0.54	0.42	0.32	0.23
2.5	80	0.36	0.36	0.36	0.27	0.21

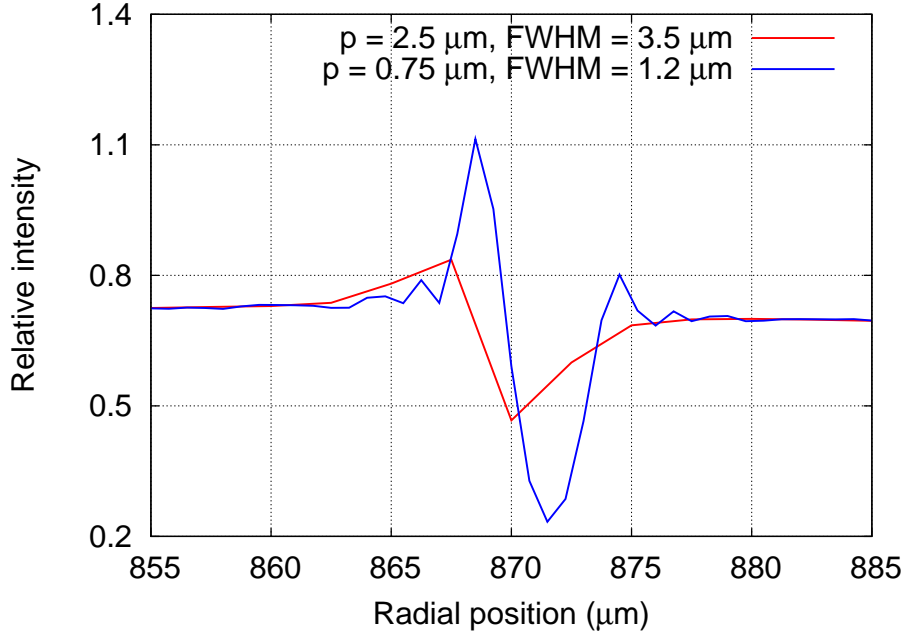


FIG. 3: Radial intensity profile for 8 keV x-rays,  $Z_{PW} = 50$  mm for pixel sizes of  $0.75 \mu\text{m}$  and  $2.5 \mu\text{m}$  with the appropriate FWHM.

#### A. Selection of a microscope objective

Several factors contribute to limiting the image resolution for the optical case, including the diffraction limit, depth of field, and higher order aberrations. The full-width at half-maximum

(FWHM) limit to the resolution is a combination of the terms

$$R_T = \sqrt{R_{PB}^2 + R_D^2 + R_F^2 + R_A^2}, \quad (5)$$

where  $R_{PB}$  is the FWHM of the penumbral blur,  $R_D$  is the diffraction limited performance,  $R_F$  is due to the depth of field, and  $R_A$  is due to higher order lens aberrations. The penumbral blur for a given geometric magnification is given by Eq. 2. Each of the optical terms, calculated based on the microscope objective, must be referenced to the object plane, and hence, divided by the geometric magnification.

The diffraction limited performance is based on the numerical aperture, NA, given by

$$R_D = 0.61\lambda / (NA * M_g), \quad (6)$$

where  $\lambda$  is the wavelength of the light emitted by the scintillator and the resolution is referenced to the object plane.

Analysis of the depth of field for several microscope objectives was performed. It was found that the modulation transfer function (MTF) was reduced by about 6% over the 30  $\mu\text{m}$  thickness of the CsI scintillator using a microscope objective with NA = 0.25. The MTF was significantly degraded using a NA = 0.45 objective. Thus, the microscope objective should be limited to an NA not greater than 0.3 with a 20-30  $\mu\text{m}$  thick scintillator for best performance.

Microscope objectives are typically well corrected for aberrations that would affect the image contrast. While low mode image distortions may be present and would need to be addressed, they will not significantly change the interface contrast. Therefore, they will be neglected in the remaining calculations.

## V. COMPARISON OF DIRECT-DETECTION WITH TWO DIFFERENT SCINTILLATOR DESIGNS

Three different imaging designs consistent with characterization of NIF capsules will be considered. The first is the direct-detection imaging method, where a CCD itself detects to x-ray photons. The second and third are low and high magnification scintillator based designs. The source is assumed to be a Cu-anode micro-focus source with 5  $\mu\text{m}$  FWHM spot size. The relative signal-to-noise at the D-T interface for the three cases will be calculated. From this, the integration time required to achieve identical statistics will be calculated.

TABLE V: Signal at D-T solid–vapor interface for 30  $\mu\text{m}$  Si and 20  $\mu\text{m}$  CsI detectors using the Cu-anode spectrum and 5 different FWHM values.

	FWHM ( $\mu\text{m}$ )				
	1.2	2.3	3.5	4.7	5.9
30 $\mu\text{m}$ Si	0.18	0.18	0.16	0.135	0.10
20 $\mu\text{m}$ CsI	0.16	0.16	0.152	0.115	0.09

### A. Direct detection

Direct-detection using a Si CCD camera is straight-forward to calculate. The CCD is assumed to be 1024x1024 and have a pixel size of 20  $\mu\text{m}$ . Thus  $M_g = 8$  is required for a 2.5 mm field of view. The penumbral blur for  $M_g = 8$  is 4.4  $\mu\text{m}$  FWHM. The calculated D-T solid–vapor interface signal using the Cu anode spectrum, 505 mm of air, and the Si energy-dependent absorption is 0.22. Our experience with the Cu-anode source was that 120 second exposure time was required to obtain an image with sufficient signal-to-noise for analysis. This exposure time corresponds to between 3000-4000 x-ray photons/pixel.

It should be noted that for this geometry with  $M_g = 8$ , the penumbral blur is 0.875  $a$ . Table IV shows that for the direct-detection geometry, there is little gain in contrast for a penumbral blur less than 3.5  $\mu\text{m}$  FWHM. Thus, an x-ray source size of 4  $\mu\text{m}$  is optimum for the direct-detection imaging system.

### B. CsI Scintillator

The CsI scintillator performance for two different magnifications are considered. The first is a full-field of view and the second is a higher magnification used to focus on defects in the ice layer such as cracks. The full-field of view uses a 1024x1024 visible light CCD chip with 25  $\mu\text{m}$  pixels. There are a number of combinations of  $M_g$  and  $M_o$  which will produce the required 10x total magnification. Table VI shows the FWHM and collection efficiency for 4 different microscope objectives. Table IV showed that the signal does increase for a FWHM less than 3.5  $\mu\text{m}$  with  $p_o = 2.5 \mu\text{m}$  pixels, which is just under the 3.6  $\mu\text{m}$  for the  $M_g = 2$ ,  $M_o = 5$  case. Thus, the best choice to maximize the contrast and the collection efficiency is for  $M_g = 2$ ,  $M_o$

= 5.

TABLE VI: Resolution and collection efficiency to obtain a total 10x magnification using commercial microscope objectives. The  $M_g = 2$ ,  $M_o = 5$  combination is the optimum for maximizing the signal and collection efficiency.

$M_o$	NA	$M_g$	$R_{PB}$ ( $\mu\text{m}$ )	$R_D$ ( $\mu\text{m}$ )	$R_D/M_g$ ( $\mu\text{m}$ )	FWHM ( $\mu\text{m}$ )	$\Omega_x \Omega_v$ ( $\times 10^{-4}$ )
1.5	0.045	6.67	4.25	7.4	1.12	4.4	3.66
2.5	0.075	4	3.75	4.47	1.12	3.9	7.91
5	0.15	2	2.5	2.23	1.12	2.7	14.1
10	0.30	1.1	0.45	1.12	1.02	1.1	1.86

The penumbral blur is  $2.5 \mu\text{m}$  FWHM. A typical NA for a 5x Nikon microscope objective is 0.15. The diffraction limited performance adds a FWHM of  $1.12 \mu\text{m}$  at the object plane. When added in quadrature, the resulting FWHM for the entire system is  $2.7 \mu\text{m}$ . The CsI is taken to be  $20 \mu\text{m}$  thick for the purpose of calculation. The calculated contrast at the D-T solid-vapor interface is 0.16 for these parameters, including the Cu-anode spectrum, 150 mm air, and CsI response. With these parameters, the performance of the scintillator system compared to the direct-detection can now be made.

The relative signal-to-noise of the direct-detection and scintillator systems are calculated based on the interface signal level and the total number of collected x-ray photons. The relative number of detected x-ray photons is given by

$$\frac{N^S}{N^D} = \left( \frac{\Omega_x^S}{\Omega_x^D} \right) \left( \frac{\eta^S}{\eta^D} \right). \quad (7)$$

Again,  $\Omega_x$  is the solid angle that a pixel subtends from the source,  $\eta$  is the relative number of photons absorbed by the detectors. The values for  $\eta$  in Table II are appropriate for vacuum propagation. When the imaging is performed in air, the energy dependent transmission through the air and the absorption at the detector must both be included.

The ratio of the signal-to-noise is given by

$$\frac{\delta^S \sqrt{N^S}}{\delta^D \sqrt{N^D}}. \quad (8)$$

For the direct-detection and CsI scintillator in vacuum, the signal-to-noise ratio is

$$\begin{aligned} & \frac{0.16}{0.16} \sqrt{(0.3265) (2.35)} \\ & = 1 \sqrt{0.77} = 0.88. \end{aligned} \quad (9)$$

This means that the exposure time for the scintillator must be  $1/0.88^2 = 1.3$  times longer than for the direct-detection for identical signal-to-noise. For measurements in air, the signal-to-noise is

$$\begin{aligned} & \frac{0.16}{0.22} \sqrt{(0.3265) (4.85)} \\ & = 0.73 \sqrt{1.58} = 0.92. \end{aligned} \quad (10)$$

The signal is stronger of the direct-detection because the longer air path filters the low energy x-rays. However, the relative number of collected x-rays is reduced by transmission losses in air. The net result is that in air, the exposure time for the scintillator is 1.18 times longer than the direct-detection to obtain identical signal-to-noise. Thus, we see that there is little difference between the two methods either in air, or in vacuum.

### C. High resolution imaging of local defects

The second scintillator case to consider is for a 20x microscope objective. This would be used in the laboratory to quantify local defects on the ice layer. The contrast of multiple local defect sizes will be compared between the full field of view, or low resolution case, and the high resolution case. For this comparison, a 0.3 NA Nikon objective is assumed for the high resolution detector. The diffraction limited performance gives a FWHM of  $1.12 \mu\text{m}$ . The geometric magnification reduces this to  $0.93 \mu\text{m}$ . The penumbral blur is  $0.833 \mu\text{m}$ . Added together in quadrature, the FWHM is  $1.25 \mu\text{m}$ . The pixel size at the shell is  $1.04 \mu\text{m}$ .

A triangular crack of depth  $d$  and width  $w$  was modeled on the inner D-T ice surface. The model used monochromatic 8 keV x-rays and  $Z_{PW} = 50 \text{ mm}$ . Figure 4 shows two different crack sizes as imaged by the high and low resolution detectors. The cracks would be barely visible with the low resolution system, while the high resolution system could image the  $d = 3 \mu\text{m} \times w = 10 \mu\text{m}$  crack. Cracks of depth  $d = 20 \mu\text{m}$  are about the smallest possible with the low resolution system. Decreasing the pixel size at the object to  $0.5 \mu\text{m}$  does not significantly increase the crack contrast because of the weak D-T refractive index.

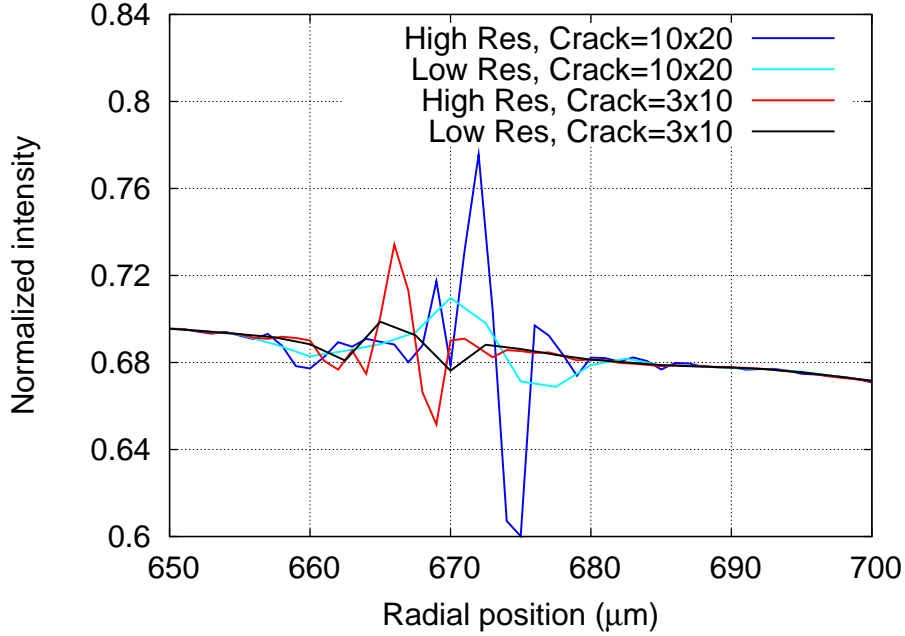


FIG. 4: Two different sized triangular cracks,  $d=10\text{ }\mu\text{m} \times w = 20\text{ }\mu\text{m}$  and  $d = 3\text{ }\mu\text{m} \times w = 10\text{ }\mu\text{m}$  imaged by the high and low resolution detectors. Monochromatic 8 keV x-rays and  $Z_{PW} = 50\text{ mm}$  were used in the calculation. The larger crack would have about 3 % contrast imaged with the low resolution system and would be barely visible in an actual image. The high resolution case would provide 6 % and 13 % contrast for the small and large cracks, respectively.

## VI. CONCLUSIONS

Direct-detection and a scintillator based system have comparable performance in phase-contrast enhanced x-ray imaging, provided the scintillator and associated optics are optimized. Thus, the choice between the methods should be based on practical considerations, such as relative cost, space requirements, and set-up difficulty. If small local defects are of interest, then a scintillator is required for high resolution imaging. There are also two other important factors that have not yet been considered because of limited data and are discussed here briefly.

The first is the possible damage to the direct-detection CCD. There is no clear guidance from the vendors on this point, however, a rough estimate was that damage begins to be noticeable with 2,500 full images. With this expected lifetime and the approximately \$10k - \$15k CCD chip replacement cost, the CCD damage is a very minor issue for NIF ignition layer characterization. However, it becomes more important for our laboratory investigations, where

approximately 100 images are taken while a single D-T layer grows and is cooled. In this case, detectable damage may occur after about 2 months of experiments.

The second factor to consider is flash x-ray sources, such as the X-pinch. The CCD well depth is filled by 200 8 keV x-rays in direct detection. This is not a problem for continuous sources as multiple exposures can easily be taken. However, the X-pinch would provide a single flash. In this case a scintillator would be the best choice to maximize the signal to noise.



**Distribution:**

Maurice Aufderheide L-096

Anton Barty L-210

Don Bittner L-481

Bill Brown L-333

Bob Cook L-481

Janelle Gunther L-399

Bruce Hammel L-481

Jeff Koch L-481

Bernie Kozioziemski L-472

Otto Landen L-481

Steve Letts L-474

Richard London L-030

Harry Martz L-151

John Moody L-481

Jorge Sanchez L-481

Jim Sater L-481

Dan Schneberk L-333

David Montgomery LANL

David Harding LLE

Haibo Huang GA

Joe Kilkenny GA

Abbas Nikroo GA

Rich Stevens GA

Wenbng Yun XRadia